# Enhancing Heat Capacity of Colloidal Suspension Using Nanoscale Encapsulated Phase-Change Materials for Heat Transfer

**Yan Hong,[†,‡] Shujiang Ding,[†] Wei Wu, Jianjun Hu,[§] Andrey A. Voevodin,[§] Lois Gschwender,[§] Ed. Snyder,[§] Louis Chow,[‡] and Ming Su*[,†,‡]**

NanoScience Technology Center and Department of Mechanical, Materials and Aerospace Engineering, University of Central Florida, Orlando, Florida 32826, and Materials and Manufacturing Directorate, Air Force Research Laboratory, Wright-Patterson Air Force Base, Ohio 45433

**ABSTRACT** This paper describes a new method to enhance the heat-transfer property of a single-phase liquid by adding encapsulated phase-change nanoparticles (nano-PCMs), which absorb thermal energy during solid−liquid phase changes. Silica-encapsulated indium nanoparticles and polymer-encapsulated paraffin (wax) nanoparticles have been made using colloid method, and suspended into poly-α-olefin (PAO) and water for potential high- and low-temperature applications, respectively. The shells prevent leakage and agglomeration of molten phase-change materials, and enhance the dielectric properties of indium nanoparticles. The heat-transfer coefficients of PAO containing indium nanoparticles (30% by mass) and water containing paraffin nanoparticles (10% by mass) are 1.6 and 1.75 times higher than those of corresponding single-phase fluids. The structural integrity of encapsulation allows repeated use of such nanoparticles for many cycles in high heat generating devices.

**KEYWORDS:** encapsulation • phase-change nanoparticles • heat transfer • colloid suspension

Nanostructured materials have created numerous opportunities for many industrial areas (1, 2). A variety of nanoparticles with unique physical properties, including optical, magnetic, electronic, chemical, and mechanical ones, have been used either alone or as functional additives to improve performance of materials (3−11). The structure, composition, and surface property, as well as the assembly of nanoparticles, can be tuned with high level of precision to allow bottom-up construction of novel materials (12−16). Owing to their small sizes and large surface to volume ratios, nanoparticles have been added into solid or liquid media to form homogeneous mixtures with intimate contacts (17, 18). On the other hand, an area with great importance is heat transfer, in which a liquid (i.e., coolant) is used to transfer thermal energy from a hot source to a cold source (19, 20). Although many coolants have been designed for different operating ranges, the heat-transfer ability of liquid coolants is normally too low to remove large amount of thermal energy, because most liquids cannot support phonons (bond vibrations) or do not have free electrons to remove thermal energy. Enhancing the heat-transfer ability of liquids has been the target of many research topics that are intended to cool high power electronics and high power lasers (21, 22).

At constant flow rate of liquid, the heat-transfer ability depends on the thermal conductivity and heat capacity of the liquid (23). The practice of adding nanoparticles into liquid has been studied with hope that the thermal conductivity can be enhanced dramatically. But, recent experiments show no anomalous enhancements in thermal conductivity when solid nanoparticles such as copper, and alumina are added into fluid (24, 25). On the other hand, the heat-transfer efficiency depends on the heat capacity of the liquid, providing an alternate for the enhancement of heat-transfer ability of liquid (26). However, the heat capacity of pure liquid is very small, because the specific heat of liquid is not a sensitive function of temperature, and the temperature difference between hot source and cold source is small. Indium nanoparticles have been added into a single-phase liquid to enhance its heat adsorbing ability (27). But, the colloid suspension of bare indium nanoparticles has limited uses in heat transfer due to several reasons: the nanoparticles have fixed melting point that cannot satisfy cooling need at different temperature; molten nanoparticles will aggregate and precipitate out of fluid during multiple melting-crystallizing processes; the metallic nanoparticles reduce dielectric property of liquid, which limits its applications in areas such as the direct immersing cooling of electronic devices, even if direct contact cooling is desired because of its minimized contact thermal resistance.

We have developed a general strategy to enhance the heat-transfer properties of liquids, where phase-change materials (i.e., metal and paraffin wax) that have appropriate thermal properties are size-reduced to be nanoparticles, encapsulated inside nonmelting shells (i.e., silica and poly-

* Corresponding author. E-mail: mingsu@mail.ucf.edu.
Received for review March 10, 2010 and accepted May 25, 2010
† NanoScience Technology Center, University of Central Florida.
‡ Department of Mechanical, Materials and Aerospace Engineering, University of Central Florida.
§ Wright-Patterson Air Force Base.
DOI: 10.1021/am100204b

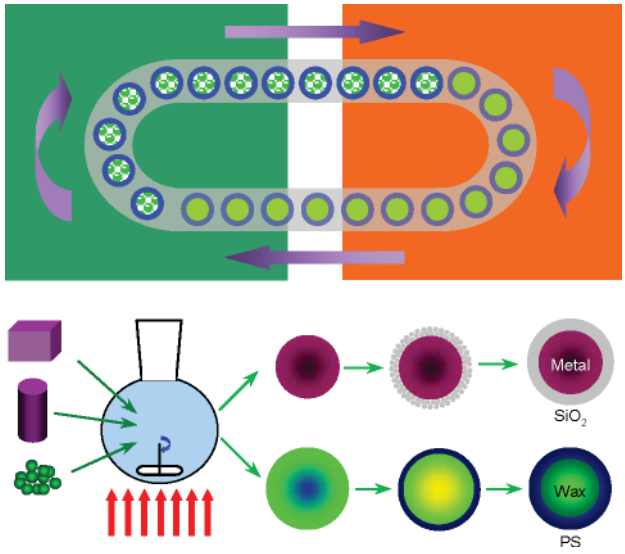


**FIGURE 1. Colloid suspension of encapsulated phase-change nanoparticles for heat transfer.**

mer), and added into liquids (i.e., poly-α-olefin and water) to enhance the heat capacities of the corresponding liquids for high- and low-temperature applications, respectively. The enhanced heat transfer of fluid containing nano-PCMs is achieved by increasing thermal conduction of fluid. During the solid−liquid phase changes, the nano-PCMs absorb thermal energy from hot source and become liquid; nonmelting shells prevent the leakage or agglomeration of molten cores; and the molten cores solidify at cold source to release thermal energy (Figure 1). The nano-PCMs have been made and encapsulated using the state-of-the-art colloidal methods. Transmission electron microscope (TEM) confirms core−shell structures of encapsulated nanoparticles. The thermo-physical properties of colloid suspension are measured by differential scanning calorimetry (DSC) and tested on a heat-transfer loop. This work is innovative for several reasons: (1) enhancement of heat transfer through latent heat is more straightforward and practical than that through the thermal conductivity; (2) nonmelting shells prevent leakage or aggregation of molten nanoparticles and reaction of nanoparticles with liquids; and (3) encapsulation of metal nanoparticles inside dielectric shells allows immersion cooling of electronic devices.

## MATERIALS AND METHODS

All chemicals used in this experiment are obtained from Aldrich without purification. Direct emulsification of appropriate precursors is used to prepare nano-PCMs of metal and paraffin wax. In the case of indium that has a melting point of 156 °C, emulsification is carried out by boiling certain amount of indium powder (−325 mesh) in poly-α-olefin (PAO) at 200 °C for 12 h with magnetic stirring under the protection of nitrogen gas. The sol−gel method is used to encapsulate nanoparticles with silica after removing nanoparticles from PAO by centrifuging (28−31). Tetraethyl-orthosilicate (TEOS) is added in an ethanolic suspension of indium nanoparticles, followed by dropwise addition of ammonium hydroxide at 60 °C. After reacting for 90 min, encapsulated nanoparticles are washed by ethanol for several times and redispersed in PAO at a certain ratio. A one-pot method is used to make polymer-encapsulated paraffin wax nanoparticles (32, 33). Briefly, 10.0 g of octadecane at melting point of 28 °C, 1.0 g of acrylate acid and 0.1 g of dodecylmercaptan are dissolved in 10.0 g of styrene by sonication for 10 min. The mixture is poured into 30.0 g of aqueous solution that contains 0.2 g of sodium dodecylsulfate and 0.2 g of Triton X-100 in a 250 mL three-neck flask. The mixture is sonicated for 10 min to form a stable emulsion. The flask is purged by nitrogen for 30 min, followed by heating at 70 °C for 12 h at 200 rpm to complete the polymerization.

The as-made encapsulated nano-PCMs have been characterized using a variety of techniques. A differential scanning calorimeter (PerkinElmer DSC7) is used to measure the thermal properties of nano-PCMs at temperature ramp rate of 2 °C/min. A Zeiss (Ultra 55) scanning electron microscope (SEM) operated at 10 keV is used to image the morphology of the nanoparticles. A TEM (JEOL 1011) operated at 100 kV is used to image the structure of the nanoparticles. High-resolution TEM (TECNAI F30) with in situ heating ability is used to study the thermal stability of silica shells. In order to prepare sample for TEM imaging, an ethanol drop containing nanoparticles is dropped on a copper TEM grid coated with carbon film. X-ray diffraction analysis (XRD) is carried out on a Rigaku 2500 diffractometer using Cu $K\alpha$ radiation (40.0 kV and 30.0 mA) at step width of 2.0°/min. To collect XRD curves, nanoparticles are glued on double-sided tape and fixed on the XRD holder. The capacitances of fluids with and without nanoparticles are determined by a LCR meter (Instek LCR-819), where L, C, and R stand for inductance, capacitance, and resistance, respectively. A self-built LCR probe with two parallel electrodes at surface area of 1 $cm^2$ and distance of 1 mm is immersed in liquid. The dielectric constants are derived from the ratios of capacitances of liquid to that of air at different frequency. The size distribution of nanoparticles is measured using dynamics light scattering (DLS, PD2000) by adding 5 $\mu$L nanoparticle suspension into 1.5 mL water in a plastic cuvette. The viscosity of fluid containing nano-PCMs is derived by comparing the times required to flow a certain volume of fluid and water through a glass capillary.

The heat-transfer properties of colloid suspensions are measured on a self-built heat loop, which consists of nano-PCM reservoir, microchannel heat exchanger, preheating unit, pump, valve, flowmeter and cooling unit. The nano-PCM suspension is pumped from the reservoir using a diaphragm pump. The valve is used to adjust the flow rate in the loop. The flow rate is measured by two rotameters with scale of 1262 and 2524 mL/min. Two mixing sections are used to disturb fluid so that temperature can be measured at the inlet and outlet of the microchannel. The cooling unit is used to cool working fluid after it leaves the test section. Two thin film resistors soldered at the bottom of microchannel heat exchanger are used as heaters. The power to resistors is supplied by a DC power supply that is adjustable to change the amount of heat generated by the heater. Two pairs of 0.3 mm Omega thermocouples are embedded in a copper slice between heaters and microchannel to measure the wall temperature. The temperatures of nano-PCM before and after entering the microchannel are measured by using two thermocouples and namely as inlet and outlet temperature. The power generated by the heater is the product of the voltage applied on the heater and current that passes through it.

## RESULTS AND DISCUSSION

**1. Structural Analysis of Encapsulated Nano-PCMs.** The melting point of indium is lower than the boiling point of PAO. Indium powder is reduced directly to nanoparticles under shear force of stirring. Figure 2A shows a SEM image of silica-encapsulated indium nanoparticles. The silica shells are smooth, showing that nucleation of silica is

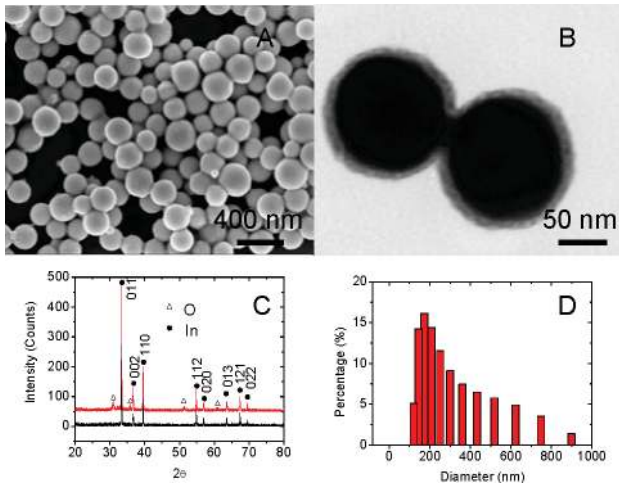


**FIGURE 2. (A) SEM and (B) TEM images of silica-encapsulated indium nanoparticles; (C) XRD spectrum and (D) size distribution of silica-encapsulated indium nanoparticles.**

initiated from surfaces of nanoparticles. Figure 2B is a bright-field TEM image of silica-encapsulated indium nanoparticles, where the diameter of nanoparticle core and thickness of silica shell can be controlled by changing reaction time or concentration of precursor. The diameters of indium nanoparticles depend on boiling time and size of starting materials (powder), and decrease from 165 to 90 nm as time increases from 2 to 48 h (Supporting Figure A). The relationship between nanoparticle size and reaction time can be fitted to Taylor's formula (34): $r_p = W_e\sigma/(\mu_c\gamma)$, where $r_p$ is the nanoparticle radius, $W_e$ is Weber number, $\sigma$ is the interfacial tension between nanoparticles and PAO, $\gamma$ is the shear rate, and $\mu_c$ is the viscosity of PAO. The thickness of silica shell can be controlled from 10 to 80 nm by changing the concentration of precursor from 0.1 to 1 mM. XRD spectra show that indium power and nanoparticles have tetragonal structures (Figure 2C), where a small oxygen peak can be found at nanoparticles, showing that indium may be slightly oxidized after boiling for more than 24 h. The size distribution of silica-encapsulated indium nanoparticles is measured by DLS. Figure 2D shows the average diameter is 200 nm with majority of nanoparticles in the range of 100−300 nm. Similarly, polystyrene-encapsulated paraffin nanoparticles have been characterized. SEM image shows the average diameter of nanoparticles is about 200 nm (Figure 3A), which is close to that measured by DLS (Figure 3C inset). TEM image (Figure 3B) shows the diameter of PCM cores and the polymer shell are 150 and 25 nm, respectively. Fourier transform infrared spectroscopy (FTIR) confirms the formation of polystyrene-encapsulated paraffin nanoparticles (Figure 3C). The two absorption peaks of spectrum (1) at 2916 and 2848 $cm^{-1}$ are the characteristic peaks of the aliphatic C−H stretching vibration, the absorption peaks at 1464 $cm^{-1}$ is assigned to the C−H bending vibration, and the peak at 721 $cm^{-1}$ is associated with the in-plane rocking vibration of the $CH_2$ group. From spectrum (2) in Figure 3C, it can be seen that there are six more peaks, the absorption peaks at 3060 and 3026 $cm^{-1}$ are associated with the aromatic C−H stretching vibration, the absorption peak at

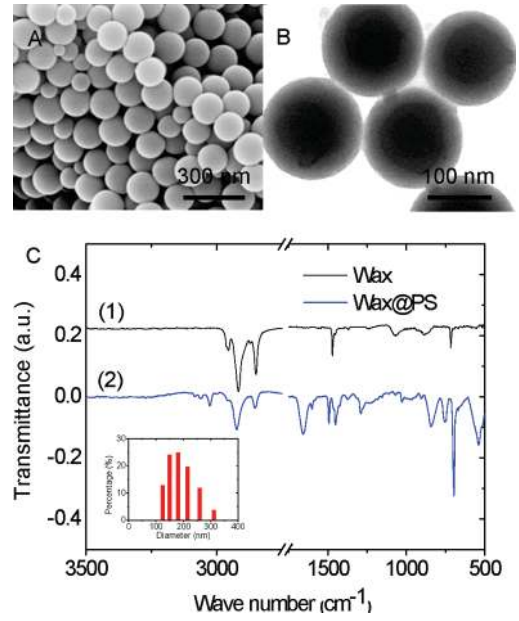


**FIGURE 3. (A) SEM and (B) TEM images of polystyrene-encapsulated paraffin nanoparticles; (C) FTIR spectra of pure paraffin (curve 1) and polystyrene-encapsulated paraffin nanoparticles (curve 2); size distribution of polymer-encapsulated paraffin nanoparticles (C, inset).**

2923 $cm^{-1}$ is associated with aliphatic C−H stretching vibration, the absorption peaks at 1601 and 1490 $cm^{-1}$ are associated with benzene ring C=C stretching vibration, and the absorption peaks at 756 and 700 $cm^{-1}$ are benzene ring deformation vibration. These peaks are assigned to polystyrene. The characteristic peaks of paraffin wax could be observed in the FTIR spectrum of the polystyrene-encapsulated paraffin nanoparticles. It is noted that the peaks of aliphatic C−H stretching vibration red shifts from 2916 and 2848 $cm^{-1}$ to 2924 and 2853 $cm^{-1}$, respectively, as a result of the interaction between paraffin core and polymer shell.

**2. Dielectric Properties of Colloid Suspension Containing Encapsulated Nanoparticles.** Depending on whether nanoparticles are conductive or not, adding nanoparticles into liquids will decrease or enhance dielectric properties of liquids. We have measured the capacitances of PAO, indium nanoparticles in PAO and silica-encapsulated indium nanoparticles suspended in PAO, in the frequency range of 12 Hz to 100 kHz. Figure 4A shows that indium nanoparticles decrease the dielectric constants of PAO, but silica-encapsulated indium nanoparticles enhance that of PAO. The dielectric constant of PAO containing silica-encapsulated indium nanoparticles reaches the maximum at ~100 Hz, whereas that of PAO containing indium nanoparticles increase from 12 to 100 Hz and remain constant up to 100 kHz. The concentration dependent dielectric constants of PAOs containing indium, and silica-encapsulated indium nanoparticles are measured at frequency of 1 kHz as shown in Figure 4B, where increasing indium content leads to a decrease in dielectric constant of PAO from 1.65 to 1.35, but increasing the content of silica-encapsulated indium nanoparticles leads to an increase in dielectric constant from 1.58 to 2.17. The dielectric property of conductive particles in a nonconductive matrix is dependent

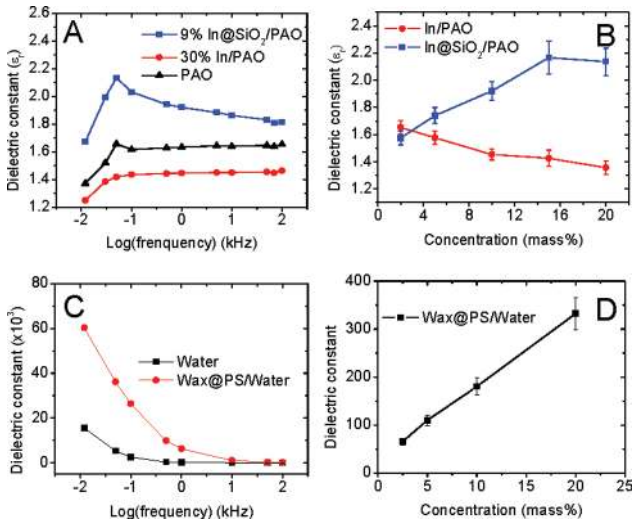


FIGURE 4. (A) Dielectric constants as function of frequencies of PAO (triangle), PAO with 30% indium nanoparticles (circle) and PAO with 9% silica-encapsulated indium nanoparticles (square); (B) dielectric constants at 1 kHz as function of the concentrations of indium (circle) and silica-encapsulated indium (square) nanoparticles in PAO; (C) dielectric constant of polystyrene-encapsulated paraffin in water as function of frequency; and (D) concentration-dependent dielectric constants of polystyrene-encapsulated paraffin nanoparticles.

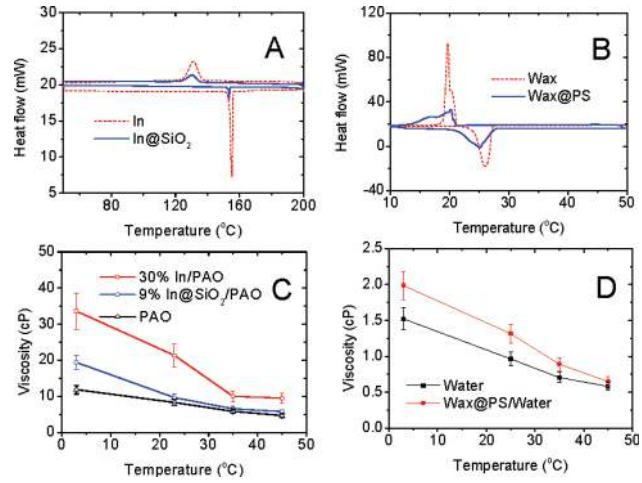


FIGURE 5. (A) DSC curves of indium nanoparticles (dash) and silica-encapsulated indium nanoparticles (solid); (B) DSC curves of paraffin (dash) and polystyrene-encapsulated paraffin nanoparticles (solid); (C) viscosities of PAO (triangle), PAO with 30% indium nanoparticle (square), and PAO with 9% silica-encapsulated indium nanoparticles (circle) as function of temperature from 3 to 45 °C; (D) viscosities of water and polystyrene-encapsulated paraffin in water as function of temperature from 3 to 45 °C.

on percolation of charges via random chains formed by the conductive particles. The percolation threshold for indium nanoparticles is at 10% of mass concentration, which is close to that for spherical conducting particles in an insulating liquid matrix (15%). The increase in dielectric constant after adding silica-encapsulated nanoparticles can be attributed to the high dielectric constant of silica (4.5). Similarly, adding polymer-encapsulated paraffin nanoparticles into water enhances the dielectric constant of water (Figure 4C), and a linear relation exists between nanoparticle concentration and measured dielectric constant (Figure 4D).

**3. Thermophysical Properties of Colloid Suspensions Containing Encapsulated Nano-PCMs.** The melting temperature and latent heat of fusion of encapsulated nano-PCMs have been studied at heating rate of 2 °C/min on DSC by adding certain amount of nanoparticles in an aluminum pan. Figure 5A shows DSC curves of indium nanoparticles and silica-encapsulated indium nanoparticles, where the melting and freezing temperatures are at 155.3 and 135 °C, respectively. The enthalpy of phase change is derived as 19.6 J/g from the area of melting peak, which is lower than that of bulk value (28.5 J/g). The difference is due to presence of silica, which does not melt unless temperature is over 1600 °C. The mass ratio of indium inside encapsulated nanoparticles is determined to be 68.8%. Figure 5B shows DSC curves of paraffin and polystyrene-encapsulated paraffin nanoparticles, where the melting and solidifying peaks of paraffin are 27.8 and 19.2 °C, respectively, close to those of encapsulated paraffin nanoparticles (27.1 and 19.6 °C), respectively. The slight peak shifts may be due to the interaction of paraffin with polymer. The enthalpy of phase change of paraffin is calculated from the melting peak as 232.3 J/g. The enthalpy measured from encapsulated paraffin is determined to be 110.05 J/g, meaning the content of paraffin is ~47.4 wt % that is close to the designed value (50% by mass).

Viscosity is an important parameter that affects the performance of colloid suspension as coolant. We have measured the viscosities of colloid suspensions by measuring times they take to flow through a capillary. Assuming the suspensions are Newtonian without kinetic energy terms, the flow time is proportional to the viscosity as follows (35)

$$\eta = \frac{\pi r_c^4 \Delta P}{8 V_f L} t = A\rho t \qquad (1)$$

where $r_c$ and $L$ are the radius and length of the capillary, $V_f$ is the volume of liquid that flows through the capillary, and $\Delta P$ is pressure difference. If gravity is the driving force for the liquid flow, $\Delta P$ is equal to $\rho gh$ where $\rho$ is the solution density and $A$ is a constant. The viscosities of PAO, PAO with indium nanoparticles, and PAO with silica-encapsulated indium nanoparticles decrease as temperature increases from 3 to 45 °C (Figure 5C). PAO with indium nanoparticles has higher viscosity than those of pure PAO and PAO with silica-encapsulated indium nanoparticles. The viscosity of PAO with silica-encapsulated indium nanoparticles at 45 °C (9.49 cP) is close to that of PAO (4.68 cP). The viscosity of water-based polymer-encapsulated paraffin nanoparticles has been measured using the same method (Figure 5D), where the viscosity of water decreases from 1.52 to 0.58 cP as temperature increases from 3 to 45 °C, and the viscosity of polystyrene-encapsulated paraffin nanoparticles decreases from 1.99 to 0.65 cP in the same temperature range. The viscosity of colloid suspension at 3 °C is 30.5% higher than water, but the difference decreases to 10.7% at 45 °C.

**4. Heat Transfer Loop Tests of Encapsulated Nano-PCMs Colloids.** The heat-transfer behaviors of encapsulated nano-PCMs colloids are studied on the heat-transfer loop, where the major part is a $2 \times 1 \times 1$ cm$^3$ heat exchanger that has 8,000 microchannels with dimensions of $25 \times 100 \times 500$ $\mu$m$^3$ (width × height × length). A 500 mL PAO with indium nanoparticles or PAO with encapsulated indium nanoparticles is pumped between a hot source and a cold source. The pressure drop at the inlet and outlet of microchannel is monitored to ensure continuous flow of nano-PCMs colloids. The heat-transfer coefficient has been defined as

$$h_1 = Q_{\text{fluid}}/A_{\text{base}}\Delta T \tag{2}$$

where $A_{\text{base}}$ is the surface area of microchannel heat exchanger, $\Delta T_{\text{m}}$ is the temperature difference between the inlet and outlet of the heat exchanger, and $Q_{\text{fluid}}$ is the heat absorbed by the fluid which is defined as

$$Q_{\text{fluid}} = mC_{\text{P}}(T_{\text{fluid,O}} - T_{\text{fluid,i}}) \tag{3}$$

Log mean temperature difference defined as

$$\Delta T_{\text{m}} = \frac{(T_{\text{w}} - T_{\text{i}}) - (T_{\text{w}} - T_0)}{\ln[(T_{\text{w}} - T_{\text{i}})/(T_{\text{w}} - T_0)]} \tag{4}$$

is also used to indicate the heat-transfer behavior, where $T_{\text{w}}$ is the temperature of copper between resistors and microchannel heat exchanger. Figure 6A shows the log mean temperature difference as the function of inlet temperature. The heat capacity of PAO with indium nanoparticles is less than that of PAO when temperature is below 140 °C; the temperature difference reaches minimum at 152 °C due to the melting of indium nanoparticles. The same trend is observed in the case of PAO with silica-encapsulated indium nanoparticles. Figure 6B shows the heat-transfer coefficient as the function of temperature. The maximal heat-transfer coefficient of PAO with 30% indium nanoparticles is 60% higher than that of PAO. In the case of PAO containing 9% silica-encapsulated indium nanoparticles, the maximal heat-transfer coefficient is 26% higher than that of PAO at 152 °C. The heat-transfer properties of encapsulated paraffin nanoparticles have been tested in the same way. Figure 6C shows the log mean temperature difference as function of inlet temperature for polystyrene-encapsulated paraffin nanoparticles, where the temperature difference reaches minimum at 24.2 °C due to the melting of paraffin nanoparticles. The maximal heat-transfer coefficient of water with 10% polystyrene-encapsulated paraffin is 75% higher than that of water alone (Figure 6D). The encapsulated PCM nanoparticles are stable after ~100 melting-crystallizing cycles. TEM images of silica-encapsulated indium nanoparticles and polystyrene-encapsulated paraffin wax nanoparticles after the loop test are shown in images E and F in Figure 6,

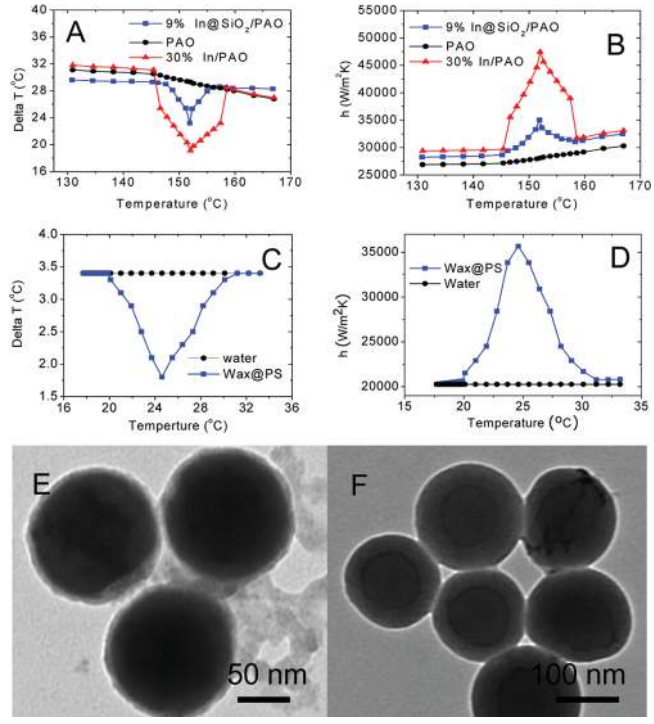


**FIGURE 6. (A) Log mean temperature difference and (B) heat-transfer coefficient of silica-encapsulated indium nanoparticles as function of temperature; (C) log mean temperature difference and (D) heat-transfer coefficient of polystyrene-encapsulated paraffin nanoparticle as function of temperature. TEM images of (E) silica-encapsulated indium nanoparticles and (F) polystyrene-encapsulated paraffin nanoparticles after the loop tests.**

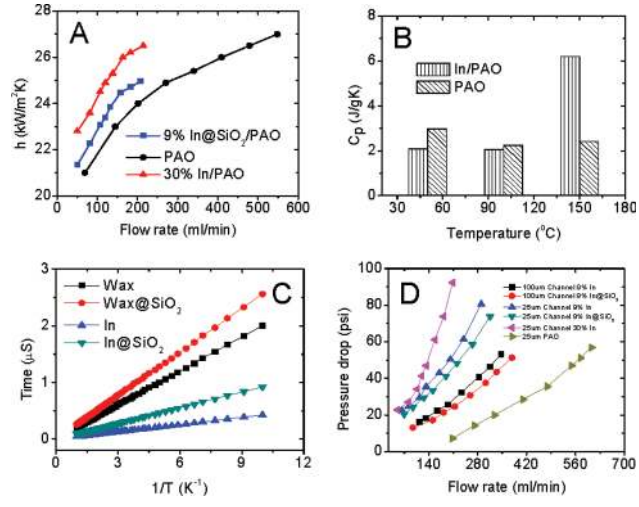


**FIGURE 7. (A) Heat transfer coefficient as function of flow rate; (B) heat capacity of indium nanoparticles as function of temperature; (C) melting times of 200 nm indium nanoparticles (and paraffin nanoparticles) with and without 20 nm shell; (D) the pressure drops of nanoparticle suspensions in microchannels as function of flow rate.**

respectively, where the core and shell structures of encapsulated nanoparticles are preserved.

**5. Melting Time of Phase-Change Nanoparticles.** To exploit the latent heat of fusion, nano-PCMs have to melt and recrystallize during the heat loop, thus flow rate and melting time will be important parameters. Figure 7A shows the heat-transfer coefficient as a function of flow rates of PAO, PAO with 30% indium nanoparticles, and PAO with

9% silica-encapsulated indium nanoparticles. At the same flow rate, PAO containing 30% nanoparticles has higher heat-transfer coefficient than PAO itself or PAO containing 9% silica-encapsulated indium nanoparticles. The heat capacity of 30% In/PAO nano-PCMs colloid is 3 times higher than pure PAO, which has been confirmed by the large specific heat of PAO with indium nanoparticles at 150 °C (Figure 7B). At a flow rate of 210 mL/min, the resident time of nanoparticles inside a 500 $\mu$m long heat source is 2 ms.

Heat absorption of particles is determined by characteristics of heat conduction within particles, which in turn depends upon the particle size and material properties. Heat transfer from the fluid to the particles is controlled by the difference between fluid temperature and the surface temperature of the particles. The surface temperature determines heat transfer within the particles. Consider a solid particle at phase-change temperature $T_m$. Neglecting the sensible heat capacity, the heat absorbed at the interface must be conducted through the liquid to the solid and is described by (36)

$$\ddot{q} = \frac{4\pi k_l (T_s - T_m)}{1/r - 1/r_P} \tag{5}$$

where $T_s$ and $T_m$ are the surface temperature and the melting point of nanoparticles, respectively; $r_p$ is the radius of the nanoparticles before melting, and $k_l$ is the thermal conductivity of nanoparticles. In addition, neglecting the sensible heat capacity, the heat absorbed at the interface must be conducted through the liquid to the solids, which means

$$\ddot{q} = \dot{m} Q_L = (\rho_l 4\pi r^2 dr) Q_l \tag{6}$$

where $\rho_l$ is the density of nanoparticles, and $Q_l$ is the latent heat of fusion of the nanoparticles. Combining eqs 5 and 6 and integrating gives

$$\frac{4\pi k_l (T_s - T_m)}{\left(\frac{1}{r} - \frac{1}{r_p}\right)} = \rho_l Q_l 4\pi r^2 \left(-\frac{dr}{d\tau}\right) \tag{7}$$

where $\tau$ is the melting time when the solid radius is $r$. The melting time is dependent on size and temperature difference between the surface temperature of the nanoparticle and the melting temperature of the nanoparticle material

$$\frac{(T_s - T_m)\tau}{\left(\frac{\rho_l Q_l}{k_l}\right)} = r_p^2 \left[\frac{1}{3}\left(\frac{r}{r_p}\right)^3 - \frac{1}{2}\left(\frac{r}{r_p}\right)^2 + \frac{1}{6}\right] \tag{8}$$

In the case of silica-encapsulated nanoparticles, silica shell has a lower thermal conductivity (1.3 W/mK) than that of metallic material, eq 7 is modified to include the contribution the silica shell

$$\frac{(T_s - T_m)}{R_{In} + R_{SiO_2}} = 4\pi \rho_{In} Q_{In} r^2 \left(-\frac{dr}{d\tau}\right) \tag{9}$$

$$R_{In} = \frac{1}{4\pi k_{In}}\left(\frac{1}{r} - \frac{1}{r_{In}}\right), R_{SiO_2} = \frac{1}{4\pi k_{SiO_2}}\left(\frac{1}{r_{In}} - \frac{1}{r_{SiO_2}}\right)$$

Integrating eq 9 gives

$$\tau(T_s - T_m) = \rho_{In} Q_{In}\left[\frac{1}{3}\left(\frac{1}{k_{In} r_{In}} + \frac{1}{k_{SiO_2} r_{SiO_2}} - \frac{1}{k_{SiO_2} r_{In}}\right) r^3 - \frac{1}{2}\frac{r^2}{k_{In}} + \frac{1}{6}\frac{r_{In}^2}{k_{In}} - \frac{1}{3}\frac{r_{In}^3}{k_{SiO_2} r_{SiO_2}} + \frac{r_{In}^2}{3k_{SiO_2}}\right] \tag{10}$$

where $k_{In}$ and $k_{SiO_2}$ are 81.8 and 1.3 W/(m K), respectively, $r_{In}$ and $r_{SiO_2}$ are 100 and 120 nm, respectively, $Q_{In}$ is 28.52 J/g, and $\rho_{In}$ is 7.3 g/cm$^3$. Replace all symbols with numbers and let $r$ equal to 0 nm, eq 10 can be rewritten as

$$\tau(T_s - T_m) = 0.92 \times 10^{-7}\ \text{s K} \tag{11}$$

Figure 7C shows the melting time as the function of temperature difference between surface temperature and melting temperature. The melting time $\tau$ is 0.92 $\mu$s when $T_s - T_m$= 0.1 K, which is two times than that of bare indium nanoparticles (0.44 $\mu$s from eq 8). But, there is still enough time at the flow rate of 210 mL/min (2 ms) for indium nanoparticles to melt even if the shell thickness is 1000 nm (melting time 4.83 $\mu$s). In case of polymer-encapsulated paraffin nanoparticles, both $k_{Wax}$ and $k_{shell}$ are taken as 0.15 W/(m K), $r_{Wax}$ and $r_{shell}$ are 100 and 120 nm, respectively, $Q_{Wax}$ is 232 J/g, and $\rho_{Wax}$ is 0.7 g/cm$^3$. The melting equation can be written as

$$\tau(T_s - T_m) = 2.56 \times 10^{-6}\ \text{s K} \tag{12}$$

The melting time of polystyrene-encapsulated paraffin nanoparticles is 25.6 $\mu$s when $T_s - T_m$= 0.1 K. Therefore, there is enough resident time at a flow rate of 210 mL/min (2 ms) for paraffin nanoparticles to melt.

An important parameter is pressure drop between the inlet and the outlet of microchannel heat exchanger. In ideal case, the pressure drop should be as small as possible to minimize pumping power. However, the pressure drop of PAO with 30% indium nanoparticles is up to seven times higher than that of pure PAO at the same flow rate. While the pressure drop of PAO with 9% silica-encapsulated indium nanoparticles is about four times higher than that of pure PAO at the same flow rate. The pressure drop of PAO with 9% indium nanoparticles is about 10% higher than that with 9% silica-encapsulated indium nanoparticles (Figure 7D). If the viscosity of suspension is the only cause for pressure drop, the pressure drop of PAO with nanoparticles

should be 10−20% more than that of pure PAO, because the effective viscosity of colloid suspension is 10−20% higher than that of PAO. The observed high pressure drop is most likely due to channel clogging. Furthermore, we have repeated the loop test on large microchannels (100 $\mu$m), the pressure drop is much smaller. Our recent experiments on jet impingement spray cooling with large diameter of nozzle have shown much smaller pressure drop (30−40%). At last, encapsulated nanoparticles show supercooling behaviors: indium nanoparticles show 20−30 °C difference in melting and crystallizing peaks; and polystyrene-encapsulated paraffin nanoparticles show 5−7 °C difference. The inner surface of silica shell could be roughened to provide more nucleation sites for molten nano-PCMs.

## CONCLUSIONS

Silica-encapsulated indium nanoparticles and polystyrene-encapsulated paraffin wax nanoparticles have been made at high yield and low cost for both high temperature and low temperature heat-transfer applications. Adding such nanoparticles into single phase fluid (i.e., poly-α-olefin or water) enhances the thermophysical properties (i.e., heat transfer, heat capacity, and dielectric constant) of fluids. The fast melting of encapsulated nanoparticles allows complete utilization of latent heats during phase changes. The colloid suspension of encapsulated nanoparticles with its high heat-transfer property can be used as novel coolants for direct immersion cooling of both low- and high-temperature devices.

**Acknowledgment.** This project has been supported by Air Force Research Laboratory (AFRL), and National Science Foundations (CBET 0828466). Most of the characterizations were carried out at the Materials Characterization Facility at University of Central Florida. Y.H., S.D. and W.W. made equal contributions to this work.

**Supporting Information Available:** Graph of boiling time vs nanoparticle size and TEM images (PDF). This material is available free of charge via the Internet at http://pubs.acs.org.

### REFERENCES AND NOTES

(1) Arico, A. S.; Bruce, P.; Scrosati, B.; Tarascon, J.-M.; Van Schalkwijk, W. *Nat. Mater.* **2005**, *4*, 366.
(2) Kannan, R. Y.; Salacinski, H. J.; Butler, P. E.; Seifalian, A. M. *Acc. Chem. Res.* **2005**, *38*, 879.
(3) Gittins, D. I.; Bethell, D.; Schiffrin, D. J.; Nichols, R. J. *Nature* **2000**, *408*, 67.
(4) Trindade, T.; O'Brien, P.; Pickett, N. L. *Chem. Mater.* **2001**, *13*, 3843.
(5) Graf, C.; Van Blaaderen, A. *Langmuir* **2002**, *18*, 524.
(6) Velikov, K. P.; Moroz, A.; Van Blaaderen, A. *Appl. Phys. Lett.* **2002**, *80*, 49.
(7) Daniel, M.-C.; Astruc, D. *Chem. Rev.* **2004**, *104*, 293.
(8) Gao, J.; Gu, H.; Xu, B. *Acc. Chem. Res.* **2009**, *42*, 1097.
(9) Lu, A. H.; Salabas, E. L.; Schüth, F. *Angew. Chem., Int. Ed.* **2007**, *46*, 1222.
(10) Elghanian, R.; Storhoff, J. J.; Mucic, R. C.; Letsinger, R. L.; Mirkin, C. A. *Science* **1997**, *277*, 1078.
(11) Faucheu, J.; Gauthier, C.; Chazeau, L.; Cavaillé, J.-Y.; Mellon, V.; Lami, E. B. *Polymer* **2010**, *51*, 6.
(12) Hoeppener, S.; Maoz, R.; Cohen, S. R.; Chi, L. F.; Fuchs, H.; Sagiv, J. *Adv. Mater.* **2002**, *14*, 1036.
(13) Wang, Y.; Xia, Y. *Nano Lett.* **2004**, *4*, 2047.
(14) Schmid, G.; Corain, B. *Eur. J. Inorg. Chem.* **2003**, *2003*, 3081.
(15) Cairns, D. B.; Khan, M. A.; Perruchot, C.; Riede, A.; Armes, S. P. *Chem. Mater.* **2003**, *15*, 233.
(16) Zhang, J.; Tang, Y.; Weng, L.; Ouyang, M. *Nano Lett.* **2009**, *9*, 4061.
(17) Richardson, H. H.; Carlson, M. T.; Tandler, P. J.; Hernandez, P.; Govorov, A. O. *Nano Lett.* **2009**, *9*, 1139.
(18) Suryawanshi, C. N.; Lin, C.-T. *ACS Appl. Mater. Interface* **2009**, *1*, 1334.
(19) Goel, M.; Roy, S. K.; Sengupta, S. *Int. J. Heat Mass Transfer* **1994**, *37*, 593.
(20) Roy, S. K.; Avanic, B. L. *Int. Commun. Heat Mass Transfer* **1997**, *24*, 653.
(21) Yamagishi, Y.; Takeuchi, H.; Pyatenko, A. T.; Kayukawa, N. *AIChE J.* **1999**, *45*, 696.
(22) Ma, K. Q.; Liu, J. *Phys. Lett. A* **2007**, *361*, 252.
(23) Shalkevich, N.; Escher, W.; Burgi, T.; Michel, B.; Si-Ahmed, L.; Poulikakos, D. *Langmuir* **2010**, *26*, 663.
(24) Keblinski, P.; Prasher, R.; Eapen, J. *J. Nanopart. Res.* **2008**, *10*, 1089.
(25) Gao, J. W.; Zheng, R. T.; Ohtani, H.; Zhu, D. S.; Chen, G. *Nano Lett.* **2009**, *9*, 4128.
(26) Khodadadi, J. M.; Hosseinizadeh, S. F. *Int. Commun. Heat Mass Transfer* **2007**, *34*, 534.
(27) Han, Z. H.; Cao, F. Y.; Yang, B. *Appl. Phys. Lett.* **2008**, *92*, 243104.
(28) Graf, C.; Vossen, D. L. J.; Imhof, A.; Van Blaaderen, A. *Langmuir* **2003**, *19*, 6693.
(29) Liz-Marzán, L. M.; Giersig, M.; Mulvaney, P. *Langmuir* **1996**, *12*, 4329.
(30) Pastoriza-Statos, I.; Koktysh, D. S.; Mamedov, A. A.; Giersig, M.; Kotov, N. A.; Liz-marzan, L. M. *Langmuir* **2000**, *16*, 2731–2735.
(31) Morel, A.-L.; Nikitenko, S. I.; Gionnet, K.; Wattiaux, A.; Lai-Kee-Him, J.; Labrugere, C.; Chevalier, B.; Deleris, G.; Petibois, C.; Brisson, A.; Simonoff, M. *ACS Nano* **2008**, *2*, 847.
(32) Tiarks, F.; Landfester, K.; Antonietti, M. *Langmuir* **2001**, *17*, 908.
(33) Jin, Z.; Wang, Y.; Liu, J.; Yang, Z. *Polymer* **2008**, *49*, 2903.
(34) Tan, L. P.; Yue, C. Y.; Tam, K. C.; Lam, Y. C.; Hu, X. *Polymer Int.* **2002**, *51*, 398.
(35) Digilov, R. M.; Reiner, M. *Rev. Sci. Instrum.* **2007**, *78*, 035112.
(36) Incropera, F. P.; DeWitt, D. P. *Introduction to Heat Transfer*, 3rd ed.; John Wiley & Sons: New York, 1996.

AM100204B